



# Spray-hydrolytic synthesis of highly photoactive mesoporous anatase nanospheres for the photocatalytic degradation of toluene in air

Minghua Zhou<sup>a,b</sup>, Jiaguo Yu<sup>a,\*</sup>, Shengwei Liu<sup>a</sup>, Pengcheng Zhai<sup>a</sup>, Baibiao Huang<sup>c</sup>

<sup>a</sup> State Key Laboratory of Advanced Technology for Material Synthesis and Processing, Wuhan University of Technology, Wuhan 430070, PR China

<sup>b</sup> Staff Room of Chemistry, Yunyang Medical College, Shiyan 442000, Hubei, PR China

<sup>c</sup> State Key Laboratory of Crystal Materials, Shandong University, Jinan 250100, PR China

## ARTICLE INFO

### Article history:

Received 28 September 2008

Received in revised form 21 November 2008

Accepted 29 November 2008

Available online 6 December 2008

### Keywords:

Titania  
Mesoporous  
Nanospheres  
Spray hydrolysis  
Photocatalytic activity  
Photocurrent  
Toluene

## ABSTRACT

Mesoporous titania nanospheres with high specific surface area and good photocatalytic activity were fabricated on a large scale by a simple spray-hydrolytic method at 90 °C. The as-prepared TiO<sub>2</sub> spherical powders were characterized by X-ray diffraction, N<sub>2</sub> adsorption–desorption measurements, field emission scanning electron microscope, transmission electron microscopy, UV–visible diffuse reflectance spectra and photocurrent measurements. The photocatalytic activity was evaluated by photocatalytic decomposition of toluene in air. The effects of calcination temperatures on the microstructures and photocatalytic activity of the TiO<sub>2</sub> powders were investigated and discussed. The results revealed that a large amount of mesoporous titania nanospheres could spontaneously form by self-assembly of countless tiny TiO<sub>2</sub> primary nanoparticle during the spray hydrolysis at 90 °C. The calcination temperature exhibited a strong effect on the microstructures and photocatalytic activity of the prepared titania. The 400 °C-calcined sample showed the highest photocatalytic activity and was about two times higher than that of Degussa P25. At 600 °C, the photocatalytic activity decreased because of the destruction of bimodal mesoporous structure of the titania and the drastic decrease of specific surface areas.

© 2009 Published by Elsevier B.V.

## 1. Introduction

Since Honda and Fujishima discovered the photocatalytic splitting of water on TiO<sub>2</sub> electrodes in 1972, a great deal of attention has been focused in recent years on the development of highly active oxide semiconductor photocatalysts for their wide application in water and air purification and solar energy conversion [1–6]. Among the various oxide and non-oxide semiconductor photocatalysts, titania has proven to be the most suitable for widespread environmental applications due to its biological and chemical inertness, strong oxidizing power, cost-effectiveness, and long-term stability against photocorrosion and chemical corrosion. However, the photocatalytic activity of TiO<sub>2</sub> must be further enhanced from the viewpoint of practical use and commerce [7–9]. For achieving this purpose, titania powders with good crystallization, small crystallite size and high specific surface area are desirable to enhance the photocatalytic activity. Among the methods available for the preparation of fine TiO<sub>2</sub> powders, the

hydrolysis or precipitate methods have been widely employed due to their simple equipment required [10–12]. Usually, the samples obtained by these methods are amorphous in nature and heat-treatment temperatures higher than 400 °C are required to realize the phase transformation of amorphous to anatase. However, such high heat-treatment temperature will lead to the increase of crystallite size and the decrease of specific surface areas. To obtain highly photoactive TiO<sub>2</sub> powders, an optimal method is to reduce the temperature of the phase transformation from amorphous to anatase and to prepare TiO<sub>2</sub> powders at low temperatures. In this paper, a novel and simple method, spray hydrolysis crystallization method, was proposed for obtaining highly photoactive TiO<sub>2</sub> powders with very high specific surface area. This method can be realized by spraying the mixed solution of Ti(OC<sub>4</sub>H<sub>9</sub>)<sub>4</sub> and EtOH into hot distilled water (ca. 90 °C). Spray hydrolysis offers specific advantages for the fabrication of TiO<sub>2</sub> spherical particles on a large scale over conventional material processing techniques. The photocatalytic activity of the prepared samples was evaluated by photocatalytic oxidation decomposition of toluene in air. The effects of calcination temperatures on the microstructures and photocatalytic activity of the TiO<sub>2</sub> powders were investigated and discussed.

\* Corresponding author. Tel.: +86 27 87871029; fax: +86 27 87879468.  
E-mail addresses: [jiaguoyu@yahoo.com](mailto:jiaguoyu@yahoo.com), [yujiaguo@public.wh.hb.cn](mailto:yujiaguo@public.wh.hb.cn) (J. Yu).

## 2. Experimental

### 2.1. Synthesis

Tetrabutyl titanate ( $\text{Ti}(\text{OC}_4\text{H}_9)_4$ , TBOT) were used as precursor for the preparation of mesoporous  $\text{TiO}_2$  nanospheres. In a typical synthesis, 100 mL of mixed solution of TBOT and ethanol (volume ratio of TBOT to ethanol: 1:4) was sprayed into a 250 mL beaker containing 200 mL hot distilled water (90 °C) via a sprayer under continuous stirring. After further stirring for 1 h at 90 °C, the resultant mixed solution was aged for 24 h at room temperature. The aged wet precipitates were filtrated, rinsed with distilled water and absolute alcohol for two times. Then the precipitates were dried in a vacuum oven at 80 °C for 10 h. In order to investigate the effect of calcination on the microstructures and the photocatalytic activity of as-prepared samples, the obtained xerogel powder was calcined at 400 and 600 °C for 2 h, labeled as ST400 and ST600, respectively.

### 2.2. Characterization

X-ray diffraction (XRD) patterns obtained on a D/Max-RB X-ray diffractometer (Rigaku, Japan) using  $\text{Cu K}\alpha$  irradiation at a scan rate ( $2\theta$ ) of  $0.05^\circ \text{ s}^{-1}$  were used to determine the phase structure of the obtained samples. The average crystallite sizes of anatase were determined according to the Scherrer equation using the full width at half maximum (FWHM) data of anatase phase after correcting the instrumental broadening [9]. Morphology observation was performed on a S4800 field emission scanning electron microscope (FESEM, Hitachi, Japan). Transmission electron microscopy (TEM) and high-resolution transmission electron microscopy (HRTEM) observation were conducted using a JEM 2100F microscope at an accelerating voltage of 200 kV. The Brunauer–Emmett–Teller surface area ( $S_{\text{BET}}$ ) of the samples were analyzed by nitrogen adsorption in a Micromeritics ASAP 2020 nitrogen adsorption apparatus (USA). Uncalcined and calcined samples were degassed at 80 and 180 °C prior to nitrogen adsorption measurements, respectively. The BET surface area was determined by a multipoint BET method using the adsorption data in the relative pressure ( $P/P_0$ ) range of 0.05–0.3. Desorption isotherm was used to determine the pore size distribution via the Barret–Joyner–Halender (BJH) method, assuming a cylindrical pore modal [13]. The nitrogen adsorption volume at the relative pressure ( $P/P_0$ ) of 0.994 was used to determine the pore volume and average pore size. UV–visible absorbance spectra of as-prepared  $\text{TiO}_2$  particles were obtained for the dry-pressed disk samples with a UV–visible spectrophotometer (UV-2550, Shimadzu, Japan).  $\text{BaSO}_4$  was used as a absorption standard in the UV–visible absorbance experiment. Photocurrent measurements were carried out on an Electrochemical Station (CHI660, China). A collimated light beam from a 300 W PLS-SXE-300 xenon lamp was used for excitation of the ITO/ $\text{TiO}_2$  electrode. Integrated light intensity was measured with a UV radiometer (UV-A, made in Photoelectric Instrument Factory of Beijing Normal University) were  $30 \pm 0.1 \text{ mW/cm}^2$  (the peak intensity of 365 nm). These measurements were carried out with a standard three-electrode assembly. A ITO/ $\text{TiO}_2$  electrode, Pt plate, and Ag/AgCl electrode were used as the working, counter, and reference electrodes, respectively. The ITO/ $\text{TiO}_2$  electrode was prepared using the as-prepared  $\text{TiO}_2$  sample as  $\text{TiO}_2$  precursors via the doctor-blade method [14]. KOH (1.0 M) is used as the electrolyte and is saturated with air.

### 2.3. Measurement of photocatalytic activity

It is well-known that volatile organic compounds (VOCs) are triggering serious environmental problems such as stratospheric

ozone depletion and tropospheric ozone increase, depending on their chemical structures [15]. Furthermore, some of these volatile organic compounds in the indoor air are also arousing health disorders, such as leukemia, nausea, headache and fatigue [9]. Usually, these indoor volatile harmful gases come from the paint, plywood, particleboard and adhesives for wall clothes, which have been widely used in construction and furnishing. In order to protect environment and improve air quality, these produced VOCs must be decomposed to  $\text{CO}_2$ . Therefore, we chose toluene as a model contaminate chemical to evaluate the photocatalytic activity of as-prepared catalysts.

The photocatalytic activity experiments of the as-prepared mesoporous  $\text{TiO}_2$  samples and Degussa P25 for the oxidation of toluene in air were performed at ambient temperature using a 15 L photocatalytic reactor [8,9]. The catalysts were prepared by coating an aqueous suspension of  $\text{TiO}_2$  samples onto three dishes with a diameter of about 9.0 cm. The weight of catalysts used for each experiment was kept 0.20 g. The dishes containing catalysts were dried in an oven at 90 °C for about 2 h to evaporate the water and then cooled to room temperature before used. After  $\text{TiO}_2$ -coated dishes were placed in the reactor, a  $15 \pm 1 \mu\text{L}$  toluene was injected into the reactor with a microsyringe. The analysis of toluene, carbon dioxide, and water vapor concentration in the reactor was conducted on line with a Photoacoustic Field Gas-Monitor (INNOVA Air Tech Instruments Model 1412). The toluene vapor was allowed to reach adsorption equilibrium with catalysts in the reactor prior to UV light irradiation. The initial concentration of toluene after adsorption equilibrium was controlled at  $300 \pm 10 \text{ ppm}$ , which remained constant for about 5 min until a 15 W UV-lamp (6 cm above the dishes) in the reactor was turned on. Integrated UV intensity was measured with a UV radiometer (UV-A, made in Photoelectric Instrument Factory of Beijing Normal University) were  $2.9 \pm 0.1 \text{ mW/cm}^2$  (the peak intensity of 365 nm). The initial temperature was  $30 \pm 1^\circ \text{C}$  and each set of experiment in UV illumination was performed for 60 min. During the photocatalytic reaction, a near 7:1 ratio of carbon dioxide products to toluene destroyed was observed, and the toluene concentration decreased steadily with UV illumination time.

The photocatalytic activity of the mesoporous  $\text{TiO}_2$  nanospheres can be quantitatively evaluated by comparing the apparent reaction rate constants. In a heterogeneous solid–gas reaction, the photocatalytic degradation of toluene on the surface of mesoporous  $\text{TiO}_2$  nanospheres is a pseudo-first-order reaction and its kinetic equation may be expressed as follows [16–18]:

$$\ln \frac{c_0}{c_t} = kt$$

where  $k$  is the apparent rate constant,  $c_0$  and  $c_t$  are the initial and the reaction concentration of toluene, respectively.

## 3. Results and discussion

### 3.1. Microstructures of mesoporous titania nanosphere

The synthesis of mesoporous titania nanospheres is based on a series of self-aggregation processes under mild hydrolytic conditions in a hot water. Before calcination, the as-prepared sample consists of large number of nanospheres with diameters of ca. 70 nm and the external surface of the nanospheres is relatively smooth (see Fig. 1a). The relatively smooth external surface of those nanospheres suggests that they are composed of countless tiny primary nanoparticles [19]. This is consistent with the following XRD and TEM results. The aggregation of these tiny primary nanoparticles can produce large numbers of intra-aggregated pores, resulting in a high microporous volume (as shown in Fig. 2b). The effects of calcination temperatures on the

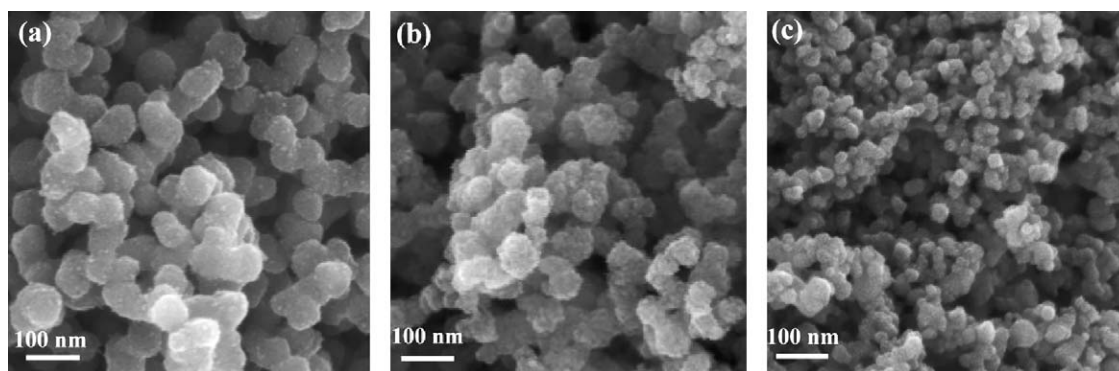


Fig. 1. FESEM images of the  $\text{TiO}_2$  powders uncalcined (a) and calcined at 400 (b) and 600 °C (c).

morphology and microstructure of the mesoporous titania nanospheres is also shown in Fig. 1. Upon calcinations, the spherical shapes are maintained, but the calcination results in shrinkages of the nanospheres and the average diameters of the nanospheres decrease from 70 to 50 (400 °C) and 35 nm (600 °C), respectively. This shrinking is caused due to collapse of smaller pores and evaporation of the physically adsorbed water and alcohol in the nanospheres. Further observation indicates that the external

surface of those nanospheres become much rougher with increasing calcination temperatures, implying that the primary building blocks of those nanospheres significantly increase in crystalline size upon calcination. The changes in primary crystalline size and particle size will further be confirmed by the following XRD and TEM analysis.

Usually, the photocatalysts with higher specific surface area and bigger pore volume are beneficial to the enhancement of photocatalytic performance due to more surface active sites for the adsorption of reactants molecules, ease transportation of reactant molecules and products through the interconnected porous networks, and enhanced harvesting of exciting light by multiple scattering within the porous framework [19]. Herein, the effects of calcination temperatures on the pore structure and BET surface areas of as-prepared samples are investigated by the adsorption–desorption measurement. Fig. 2a shows the nitrogen adsorption–desorption isotherms of the mesoporous titania nanospheres prepared by the spray hydrolysis method. Before calcination, the isotherm of the sample is a combination of type I and type IV with two very distinct regions: at low relative pressure ( $P/P_0$ ) range ( $P/P_0 < 0.2$ ), the isotherm exhibits high adsorption, indicating that the particles contain large numbers of micropores (type I) [13]. At high relative pressure ( $P/P_0$ ) range ( $0.7 < P/P_0 < 1.0$ ), the curve exhibits a hysteresis loop, indicating the presence of mesopores (type IV). The shape of the hysteresis loop is of type H3, implying the existence of slit-shaped pores [7,9,19]. After calcination, the isotherm of the sample ST400 is of type IV and contains two hysteresis loops. The shapes of two hysteresis loops are different from each other. At low relative pressure ( $P/P_0$ ) range ( $0.4 < P/P_0 < 0.7$ ), the hysteresis loop is of type H2, suggesting the presence of ink-bottle pores [13]. At high relative pressure ( $P/P_0$ ) range ( $0.8 < P/P_0 < 1.0$ ), the shape of the hysteresis loop is of type H3, suggesting the partial retention of slit-shaped pores. With increasing calcination temperature, the hysteresis loops shift to a higher relative pressure ( $P/P_0$ ) range and the areas of the hysteresis loops gradually become smaller. This indicates that the average pore size increases and the pore volume decreases with increasing calcination temperatures [9,20]. So, the isotherm of the sample ST600 only has one small hysteresis loop in the high relative pressure ( $P/P_0$ ) range ( $0.8 < P/P_0 < 1.0$ ).

The corresponding pore size distributions of the prepared  $\text{TiO}_2$  samples is shown in Fig. 2b. Before calcinations, the uncalcined sample shows the existence of micropores, mesopores and macropores [13,21]. After calcination at 400 °C, the sample ST400 contains small mesopores with a peak pore diameter of ca. 3.5 nm and larger pores with a peak pore diameter of ca. 50 nm. According to our previous works [18,19], a bimodal pore size distribution is due to two different aggregates in the powders. The smaller mesopores are usually related to primary intraagglomeration, while the larger ones are associated with secondary

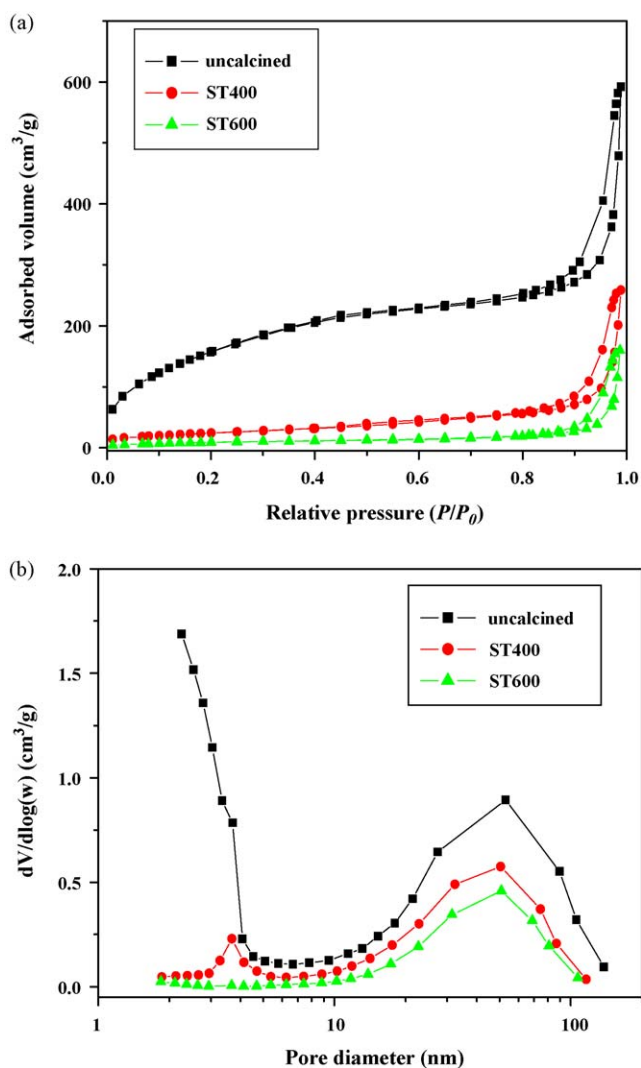


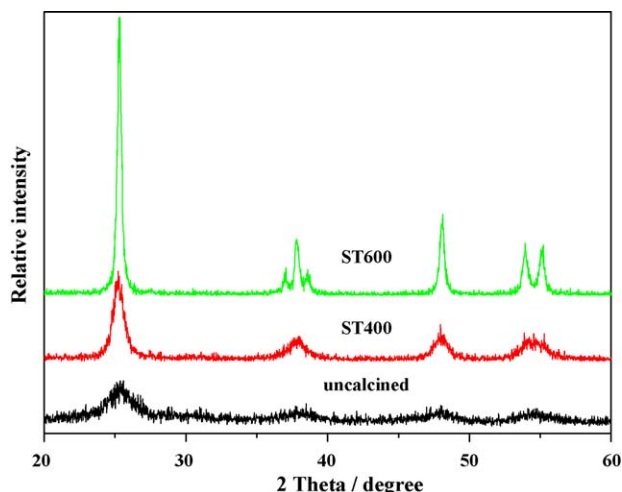
Fig. 2.  $\text{N}_2$  adsorption–desorption isotherms (a) and pore size distributions (b) of the  $\text{TiO}_2$  powders uncalcined and calcined at 400 and 600 °C.



**Table 1**Effects of calcination temperatures on the physical properties of mesoporous TiO<sub>2</sub> nanospheres.

Samples	Phase	Crystalline <sup>a</sup> size (nm)	Surface area (m <sup>2</sup> /g)	Pore volume (cm <sup>3</sup> /g)	Average pore size (nm)
Uncalcined	Anatase	6.0 (1.0)	609.6	0.56	3.7
ST400	Anatase	10.6 (2.2)	88.8	0.22	9.8
ST600	Anatase	37.6 (7.0)	33.8	0.11	12.5

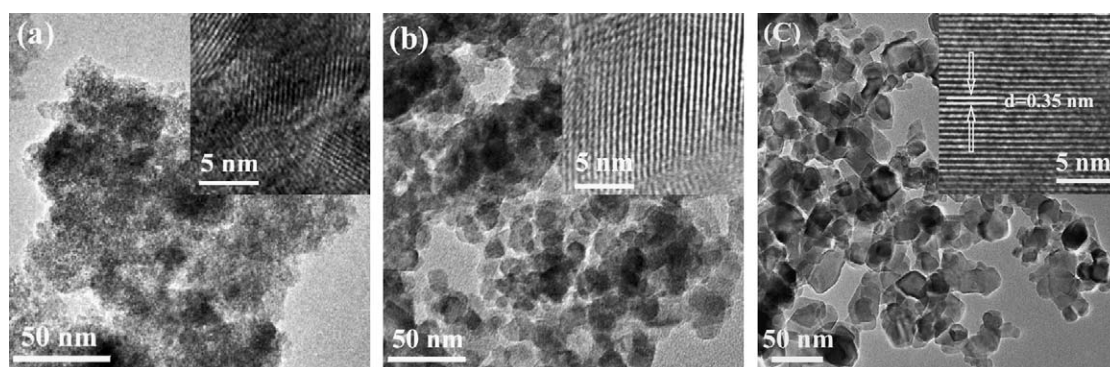
<sup>a</sup> Average crystalline size of TiO<sub>2</sub> was determined by XRD using Scherrer equation. Relative anatase crystallinity: the relative intensity of the diffraction peak from the anatase (1 0 1) plane (indicated in parentheses, reference = uncalcined sample).

**Fig. 3.** XRD patterns of the TiO<sub>2</sub> powders uncalcined and calcined at 400 and 600 °C.

interaggregation. Such bimodal pores can promote the rapid diffusion of various reactants and products during the photocatalytic reaction and enhance the rate of the photocatalytic reaction. However, the pore volume of the calcined samples decreases drastically due to the collapse of small pores during the calcination. The quantitative details about the BET surface areas, pore volume, and average pore size of the uncalcined and calcined samples are presented in Table 1. Obviously, the samples show a decrease in BET surface areas and pore volume but a increase in average pore size with increasing calcination temperatures.

Fig. 3 shows XRD patterns of the TiO<sub>2</sub> powders uncalcined and calcined at 400 and 600 °C. Before calcination, all the diffraction peaks of the uncalcined sample are in good agreement with the anatase-phase TiO<sub>2</sub> (space group: *I*<sub>4</sub>*1*/*amd* (1 4 1); JPCDS no. 21-1272) [9]. The broad diffraction peak at  $2\theta = 25.3^\circ$  corresponding to anatase (1 0 1) plane suggests its relatively smaller crystalline size, which is estimated to be ca. 6 nm by the Scherrer equation. This result is further confirmed by the corresponding TEM analysis

(Fig. 4a). Usually, the phase transformation temperature of amorphous TiO<sub>2</sub> gel to anatase is above 400 °C [18]. Why this spray hydrolysis in a hot water can induce the phase transformation at such low temperature? This is probably due to the fact that the residual unhydrolytic alkyls and organic precursors can prevent the phase transformation and crystallization of the TiO<sub>2</sub> powders by adsorbing on the surface of the primary particles. Generally, a higher hydrolysis temperature, a faster nucleophilic substituent reaction between H<sub>2</sub>O and alkoxide molecules will occur and more alkoxyl groups in the alkoxide will be substituted by hydroxyl groups of H<sub>2</sub>O [18,22]. Therefore, the decrease of the quantity of the unhydrolyzed alkyls in precursors and the increase of the hydrolytic efficiency of the alkoxide in solvents will be beneficial to the phase transformation and crystallization of TiO<sub>2</sub> gel at low temperature. Moreover, the continuous evaporation of ethanol solvent during hydrolysis and aging at 90 °C also accelerates the phase transformation and crystallization of TiO<sub>2</sub> gel. Other groups also reported similar results [23,24]. For example, Weller et al. prepared anatase TiO<sub>2</sub> nanorods by hydrolysis of titanium tetrakisopropoxide (TTIP) in oleic acid as surfactant at 80 °C, and they found that the chemical modification of TTIP by oleic acid was a rational strategy to tune the reactivity of the precursor toward water. This could ensure the formation of crystalline TiO<sub>2</sub> (anatase) via adjusting the rate of hydrolysis and condensation reactions [23]. Uekawa et al. synthesized anatase nanoparticles by heating the mixture ethanol solution of titanium isopropoxide and H<sub>2</sub>O<sub>2</sub> at 75 °C, and they also found that the heating time had strong influence on particle size, specific surface area, and photocatalytic activity [24]. Our previous results also indicated that crystalline anatase titania hollow microspheres or thin films could directly obtained using TiF<sub>4</sub> as the precursor at 60 °C and nanocrystalline TiO<sub>2</sub> powder photocatalysts were prepared by a low temperature (100 °C) solvent evaporation-induced crystallization method using tetrabutyl titanate as precursor [25–27]. While Gablenz et al. used the titanium tetrakisopropoxide as precursor to prepare fine TiO<sub>2</sub> powders via spray hydrolysis and the as-prepared sample was not crystal TiO<sub>2</sub> phase [5]. We consider that there are two factors responsible for the different results. The first one is that they used pure titanium

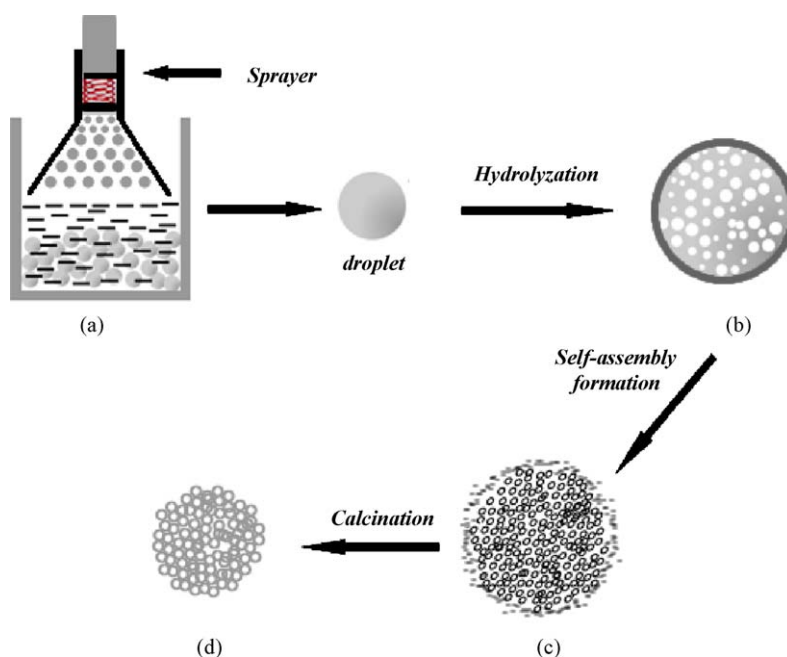
**Fig. 4.** TEM and HRTEM (inset) images of the TiO<sub>2</sub> powders uncalcined (a) and calcined at 400 (b) and 600 °C (c).

tetraisopropoxide as precursor, and the other one is that they did not age the hydrolyzed powders at the hot water. It was these two differences that resulted in the as-prepared powders appearing amorphous in their experiment. Therefore, it is not surprising that we can repeatedly obtain the anatase-phase titania nanospheres by a spray hydrolytic and aging method using dispersed TBOT as precursor in a hot water in this study. The heat-treatment not only influences the morphologies and microstructures, but also influences the crystallinity and the crystallite size of the resulting  $\text{TiO}_2$  samples [9,18–20]. After calcinations, the diffraction peak intensities obviously increase due to the enhancement of crystallization. Meanwhile, the diffraction peak width corresponding to anatase (1 0 1) plane ( $2\theta = 25.3^\circ$ ) steadily become narrower, accompanying with the increase in average anatase crystallite size from 6.0 (uncalcined) to 10.6 ( $400^\circ\text{C}$ ) and 37.6 nm ( $600^\circ\text{C}$ ) (as shown in Table 1).

TEM and HRTEM are also used to study the microstructures and crystallization of mesoporous  $\text{TiO}_2$  nanospheres. Fig. 4a shows a typical TEM image of the uncalcined sample. Because of the loose connections of the primary particles in the uncalcined sample, the nanospheres easily break into smaller particles during sample preparation of TEM via sonication, thus well-defined nanospheres are difficult to find in the TEM image. This micrograph indicates that the size of the primary particles of the uncalcined sample is quite small and is accord with the value of the crystallite size determined by XRD. These dispersed primary particles are not well crystallized, as evidenced by the uncontinuous lattice fringes (see inset of Fig. 4a). Further observation indicates that a large numbers of pores come from the aggregation of primary particles (or crystallites). Fig. 4 also shows the corresponding HRTEM images of the prepared samples, displaying clear lattice fringes, which allow for the identification of crystallographic spacing and indicates that the uncalcined, ST400 and ST600 samples are anatase  $\text{TiO}_2$  nanocrystalline. The fringes spacing of 0.35 nm (inset in Fig. 4c) matches that of the (1 0 1) crystallographic plane of anatase  $\text{TiO}_2$  [9]. With increasing calcination temperatures, the crystallinity and the crystallite size increase. The primary particle sizes of the samples ST400 and ST600 are about  $12 \pm 2$  and  $36 \pm 2$  nm, respectively, which are consistent with the results determined by XRD (as shown in Table 1).

### 3.2. Preliminary formation mechanism

According to the above SEM and TEM observations and BET analysis, the mesoporous  $\text{TiO}_2$  nanospheres can be prepared in hot water via a spray hydrolytic and aging process. The proposed mechanism for the formation of such a nanoscale spherical titania is illustrated in Scheme 1. Firstly, the precursor TBOT are well dispersed in an ethanol solution before the spray and then the mixed solution is sprayed into a hot water at about  $90^\circ\text{C}$  by a sprayer (Scheme 1a). When the fog droplets meet hot water, the ethanol molecules at the interface of the droplet are vaporized rapidly due to the fact that the temperature ( $90^\circ\text{C}$ ) of hot water is above its normal boiling point ( $78.5^\circ\text{C}$ ). Simultaneously, the interface of the droplet is covered by the hot water and then the contact between the droplets and hot water immediately produces a thin and dense semipermeable membrane at the droplet surface, as shown in Scheme 1b. This membrane will compartmentalize the subsequent hydrolysis and condensation reactions [20,28]. Then, the above reactions proceed inwardly, and the ethanol and produced butanol diffuse through the spherical outer membrane to the suspension. Subsequently, the diffusion results in the formation of microphase-separated regions (or micro/mesopores) within  $\text{TiO}_2$  nanoscale spherical particles, as shown in Scheme 1c. Although the exact and detailed formation mechanism still needs to be further investigated in our future work, we think that the ethanol plays important roles on the formation of mesoporous  $\text{TiO}_2$  nanospheres with a big micro/mesopores volume and high specific surface area. Firstly, the viscosity of TBOT is lowered and the dispersing of TBOT is enhanced with the aid of EtOH, and thus used TBOT as a precursor via the spray-hydrolytic method becomes feasibility. Secondly, the dispersed TBOT can sufficiently hydrolyze due to the fact that the dispersant, ethanol, can easily vaporize and then make the most of TBOT droplet exposure to the hot water. Thirdly, the ethanol and produced butanol within the inner of spheres will diffuse through dense semipermeable membrane into suspension due to the thermal movement or concentration difference, resulting in the formation of a large number of micro-, meso- and macropores within spherical particles because these ethanol and produced butanol molecules can be regarded as soft templates for the formation of nanopores [20].



**Scheme 1.** Schematic illustration for the formation mechanism of the mesoporous  $\text{TiO}_2$  nanospheres.

### 3.3. UV–vis diffuse reflectance spectra

Fig. 5 shows the UV–visible absorption spectra and the indirect band energy of the uncalcined and calcined samples. A significant increase in the absorption at wavelengths shorter than 400 nm can be assigned to the intrinsic band gap absorption of anatase  $\text{TiO}_2$  [9,15,29]. Usually, the heat treatment obviously affects light absorption characteristics of  $\text{TiO}_2$  [8,18,30–35]. After calcinations, an obvious red shift in the adsorption edge is observed. The blue shift associated with the uncalcined nanospheres are probably ascribed to the strong effect of Q-sized and the weaker crystallinity [4,15–16]. In contrast, the heat treatment helps to expand the wavelength response range of  $\text{TiO}_2$ , increasing the number of photo-generated electrons and holes to participate in the photocatalytic reaction [3,18], which will enhance the photocatalytic activity of the calcined samples. The red shift in the absorption edge is ascribed to the increase in crystallite sizes.

The indirect band gap energy can be estimated from a plot of  $(\alpha h\nu)^{1/2}$  versus photon energy ( $h\nu$ ). The intercept of the tangent to the plot will give a good approximation of the indirect band gap energy for  $\text{TiO}_2$ . The absorption coefficient  $\alpha$  can be calculated from the absorbance ( $A$ ) [17]. Plots of the  $(\alpha h\nu)^{1/2}$  versus photon energy ( $h\nu$ ) are shown in the Fig. 5 (inset). The indirect band gap energies estimated from the intercept of the tangents to the plots are 3.20, 3.02 and 2.96 eV for the uncalcined, ST400 and ST600 samples, respectively.

### 3.4. Photocurrent test

Fig. 6 shows the photocurrent response of mesoporous  $\text{TiO}_2$  nanospheres coated on ITO electrodes in a photoelectrochemical cell in several on–off cycles. A prompt generation of photocurrents are observed and with good reproducibility when the ITO/ $\text{TiO}_2$  electrodes are illuminated with a 300 W PLS-SXE-300 xenon lamp. While the PLS-SXE-300 xenon lamp is off, the value of photocurrent for all the ITO/ $\text{TiO}_2$  samples are instantaneously close to zero. It can be seen that the photocurrent value of the ST400 sample is the biggest among the uncalcined and calcined samples. The photocurrent values of the uncalcined and ST600 samples are 47% and 70% of that of the sample ST400, respectively. Usually, the value of photocurrent indirectly reflects the semiconductor's ability of generating and transferring of photo-generated charge carriers under irradiation [35–37]. Furthermore, the photocatalytic activity of  $\text{TiO}_2$  is highly related to the number of the separated photo-generated charge carriers [15,16]. In this respects, it can be

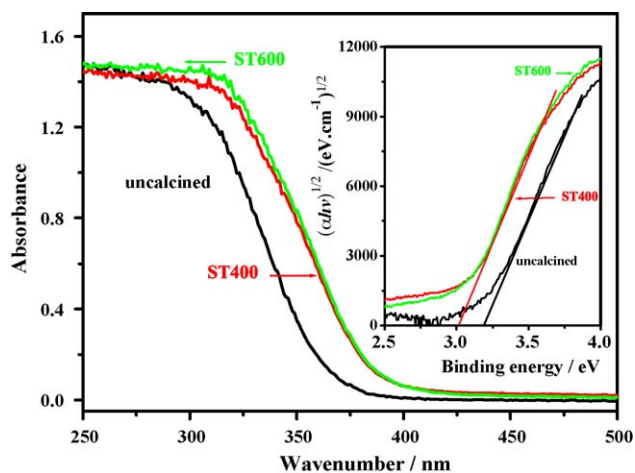


Fig. 5. UV–visible absorption spectra and the plots of the  $(\alpha h\nu)^{1/2}$  versus photon energy (inset) of the  $\text{TiO}_2$  powders uncalcined and calcined at 400 and 600 °C.

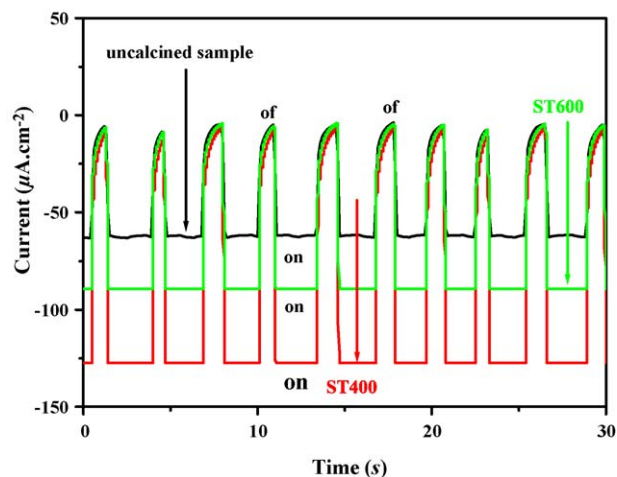


Fig. 6. Photocurrent response of the  $\text{TiO}_2$  powders uncalcined and calcined at 400 and 600 °C.

deduced that the sample ST400 will have the highest photocatalytic activity.

### 3.5. Photocatalytic activity

The photocatalytic activity of the as-prepared mesoporous  $\text{TiO}_2$  nanospheres is evaluated by the photocatalytic degradation of toluene in air. Fig. 7 shows the apparent rate constants ( $k/\text{min}^{-1}$ ) for photocatalytic oxidation of toluene under UV irradiation. It is interesting to find that the uncalcined sample has a good photocatalytic activity, and the rate constant is about  $2.2 \times 10^{-3} \text{ min}^{-1}$ , which is slightly higher than that of P25 ( $2.0 \times 10^{-3} \text{ min}^{-1}$ ). Generally, the amorphous  $\text{TiO}_2$  is not photocatalytically active, but the uncalcined sample, consisting of the mixed phase of anatase and amorphous  $\text{TiO}_2$ , shows remarkable photocatalytic activity. There are two possible reasons associated with its good photocatalytic activity. The first one is that the uncalcined sample has an especially high specific surface area ( $609 \text{ m}^2/\text{g}$ ) and large pore volume ( $0.56 \text{ cm}^3/\text{g}$ ), which is in favor of the reactant molecules to get to the active sites on its surface, hence enhancing the photocatalytic efficiency. The second one is that the uncalcined sample has biggest indirect band energy of 3.20 eV (as shown in Fig. 5), which implies that the photo-generated charge carriers of the uncalcined sample have the more

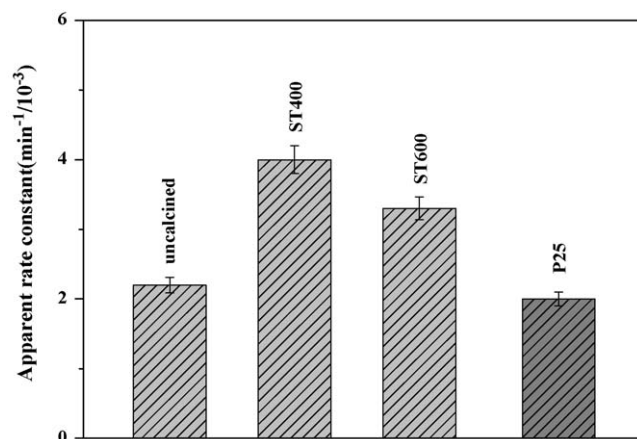


Fig. 7. Comparison of the apparent rate constants of P25, uncalcined and calcined  $\text{TiO}_2$  samples ST400 and ST600.



powerful redox ability [8,9]. Upon calcination, the photocatalytic activity increases obviously, and the rate constant reaches a maximum value at 400 °C, which is ca. two times larger than that of P25. This may be attributed to the synergetic effects of several factors such as relative crystallinity, specific surface area, and higher ability of generating and transferring of photo-generated charge carriers under UV irradiation [37–39]. It is well-known that specific surface areas and relative crystallinity are two conflicting factors influencing the photocatalytic activity of TiO<sub>2</sub>. The TiO<sub>2</sub> powders with a large surface area are usually associated with a large amounts of crystalline defects or weak crystallization, which favor the recombination of photo-generated electrons and holes, causing a low photocurrent and poor photoactivity [40–44]. Therefore, a large surface area is a requirement, but not a decisive factor. Table 1 lists effects of calcination temperatures on specific surface areas and relative anatase crystallinity of titania powders. It is interesting to note that the uncalcined sample shows very large specific surface areas, with increasing calcination temperatures, specific surface areas decrease rapidly and relative anatase crystallinity increase. Therefore, it is not surprising that the 400 °C-calcined sample shows the highest photocatalytic activity because it possesses a relative large surface area to adsorb reactant molecules and good anatase crystallinity (or lesser surface and bulk defects) to diminish the e<sup>-</sup>-h<sup>+</sup> recombination. Further increasing the calcined temperature cause a decrease in the photocatalytic activity for the sample ST600. This is due to the following two factors. Firstly, the sintering results in the destruction of bimodal mesoporous structure of the titania and the drastic decrease of specific surface area. Secondly, the relatively narrower band energy can endow the sample ST600 with the poor redox ability.

#### 4. Conclusions

Mesoporous anatase nanospherical photocatalysts could be fabricated by a spray-hydrolytic method at 90 °C using TBOT as precursor. The as-prepared sample at 90 °C had an especially high specific surface area (609 m<sup>2</sup>/g) and large pore volume (0.56 cm<sup>3</sup>/g), appeared anatase phase and showed remarkable photocatalytic activity. The calcination temperature exhibited a significant influence on morphology, particle size, specific surface areas, pore volume and photocatalytic activity of the prepared titania powders. With increasing calcination temperatures, specific surface areas and pore volume decreased, meanwhile, average crystallite size and pore size increased. All the samples prepared by this spray-hydrolytic method showed good photocatalytic activity. The 400 °C-calcined sample exhibited the highest photocatalytic activity and was about two times higher than that of Degussa P25 for photocatalytic degradation of toluene in air. At 600 °C, the photocatalytic activity of the sample decreased due to the destruction of bimodal mesoporous structure of the titania and the drastic decrease of specific surface areas.

#### Acknowledgements

This work was partially supported by the National Natural Science Foundation of China (50625208, 20773097, 20877061 and 20803055). This work was also financially supported by the National Basic Research Program of China (2007CB613302 and 2009CB939704).

#### References

- [1] K. Honda, A. Fujishima, *Nature* 238 (1972) 37.
- [2] M.A. Fox, M.T. Dulay, *Chem. Rev.* 93 (1993) 341.
- [3] M.R. Hoffmann, S.T. Martin, W. Choi, D.W. Bahnemann, *Chem. Rev.* 95 (1995) 69.
- [4] A. Fujishima, T.N. Rao, D.A. Tryk, *J. Photochem. Photobiol. C* 1 (2000) 1.
- [5] A.S. Gablenz, D. Voltzke, H.P. Abicht, J.N. Zdralek, *J. Mater. Sci. Lett.* 17 (1998) 537.
- [6] K. Nagaveni, G. Sivalingam, M.S. Hegde, G. Madras, *Environ. Sci. Technol.* 38 (2004) 1600.
- [7] J.C. Yu, J.G. Yu, W.K. Ho, Z.T. Jiang, L.Z. Zhang, *Chem. Mater.* 14 (2002) 3808.
- [8] J.G. Yu, M.H. Zhou, B. Cheng, H.G. Yu, X.J. Zhao, *J. Mol. Catal. A* 227 (2005) 75.
- [9] J.G. Yu, M.H. Zhou, B. Cheng, X.J. Zhao, *J. Mol. Catal. A* 246 (2006) 176.
- [10] N. Perkas, O. Palchik, I. Brukental, I. Nowik, Y. Gofer, Y. Koltypin, A. Gedanken, *J. Phys. Chem. B* 107 (2003) 8772.
- [11] D. Li, H. Haneda, S. Hishita, N. Ohashi, *Chem. Mater.* 17 (2005) 2588.
- [12] G.L. Messing, S. Zhang, G.V. Jayanthi, *J. Am. Ceram. Soc.* 76 (1993) 2707.
- [13] K.S.W. Sing, D.H. Everett, R.A.W. Haul, L. Moscou, R.A. Pierotti, T. Siemieniowska, *Pure Appl. Chem.* 57 (1985) 603.
- [14] A.I. Kontos, A.G. Kontos, D.S. Tsoukleris, M. Bernard, N. Spyrellis, P. Falaras, *J. Mater. Process. Technol.* 196 (2008) 234.
- [15] H. Einaga, T. Ibusuki, S. Futamura, *Environ. Sci. Technol.* 38 (2004) 285.
- [16] S. Ardizzone, C.L. Bianchi, G. Cappelletti, S. Gialanella, C. Pirola, V. Ragaini, *J. Phys. Chem. C* 111 (2007) 13222.
- [17] A. Testino, I.R. Bellobono, V. Buscaglia, C. Canevali, M. D'Arienzo, S. Polizzi, R. Scotti, F. Morazzoni, *J. Am. Chem. Soc.* 129 (2007) 3564.
- [18] J.G. Yu, G.H. Wang, B. Cheng, M.H. Zhou, *Appl. Catal. B* 69 (2007) 171.
- [19] J.G. Yu, S.W. Liu, M.H. Zhou, *J. Phys. Chem. C* 112 (2008) 2050.
- [20] J.G. Yu, Y.R. Su, B. Cheng, *Adv. Funct. Mater.* 17 (2007) 1984.
- [21] J.G. Yu, H.T. Guo, S.A. Davis, S. Mann, *Adv. Funct. Mater.* 16 (2006) 2035.
- [22] J.G. Yu, H.G. Yu, B. Cheng, X.J. Zhao, J.C. Yu, W.K. Ho, *J. Phys. Chem. B* 107 (2003) 13871.
- [23] P.D. Cozzoli, A. Kornowski, H. Weller, *J. Am. Chem. Soc.* 125 (2003) 14539.
- [24] N. Uekawa, J. Kajiwara, K. Kakegawa, Y. Sasaki, *J. Colloid Interface Sci.* 250 (2002) 285.
- [25] J.G. Yu, W. Liu, H.G. Yu, *Cryst. Growth Des.* 8 (2008) 930.
- [26] S.C. Lee, H.G. Yu, J.G. Yu, C.H. Ao, *J. Cryst. Growth* 295 (2006) 60.
- [27] J.G. Yu, J.C. Yu, *Chin. J. Chem.* 21 (2003) 994.
- [28] J.C. Yu, J.G. Yu, W.K. Ho, L.Z. Zhang, *Chem. Commun.* (2001) 1942.
- [29] W. Choi, A. Termin, M.R. Hoffmann, *J. Phys. Chem.* 98 (1994) 13669.
- [30] J. Wang, R.L. Ballesteros, T. Lopez, A. Moreno, R. Gomez, O. Novaro, X. Bokhimi, *J. Phys. Chem. B* 105 (2001) 9692.
- [31] G. Rothenberger, J. Moser, M. Graetzel, N. Serpone, D.K. Sharma, *J. Am. Chem. Soc.* 107 (1985) 8054.
- [32] T. Sakata, T. Kawai, K. Hashimoto, *Chem. Phys. Lett.* 88 (1982) 50.
- [33] N. Serpone, D. Lawless, R. Khairutdinov, *J. Phys. Chem.* 99 (1995) 16646.
- [34] A. Weibel, R. Bouchet, F. Boulc'h, P. Knauth, *Chem. Mater.* 17 (2005) 2379.
- [35] K. Inumaru, T. Kasahara, M. Yasui, S. Yamanaka, *Chem. Commun.* (2005) 2131.
- [36] F. Gao, A.J. Bard, L.D. Kispert, *J. Photochem. Photobiol. C* 130 (2000) 49.
- [37] M.D. Ward, A.J. Bard, *J. Phys. Chem.* 86 (1982) 3599.
- [38] M.H. Zhou, J.G. Yu, B. Cheng, H.G. Yu, *Mater. Chem. Phys.* 93 (2005) 159.
- [39] J.G. Yu, J.F. Xiong, B. Cheng, S.W. Liu, *Appl. Catal. B* 60 (2005) 211.
- [40] K. Tanaka, M.F.V. Capule, T. Hisanaga, *Chem. Phys. Lett.* 187 (1991) 73.
- [41] Z.B. Zhang, C.C. Wang, R. Zakaria, J.Y. Ying, *J. Phys. Chem. B* 102 (1998) 10871.
- [42] B. Ohtani, Y. Ogawa, S.I. Nishimoto, *J. Phys. Chem. B* 101 (1997) 3746.
- [43] J.G. Yu, H.G. Yu, H.T. Guo, M. Li, S. Mann, *Small* 4 (2008) 87.
- [44] J.G. Yu, X.X. Yu, *Environ. Sci. Technol.* 42 (2008) 4902.